Effects of a microscale ridge on dynamic wetting during drop impact

H. Rashidian[a], M. Broom[b], G.R. Willmott[b,c,d], M. Sellier[a]*

[a]Mechanical Engineering Department,University of Canterbury,Christchurch8041,New Zealand
[b]Department of Physics, The University of Auckland, Auckland, New Zealand
[c]School of Chemical Sciences, The University of Auckland, Auckland, New Zealand
[d]The MacDiarmid Institute for Advanced Materials and Nanotechnology

*Address all correspondence to: Mathieu Sellier, E-mail: mathieu.sellier@canterbury.ac.nz

ABSTRACT

High-speed imaging of water drop impacts on a polymer surface have been used alongside two-dimensional Lattice Boltzmann simulations to investigate the conditions under which a spreading lamella submerges a small surface ridge. Three basic outcomes have been observed when the lamella comes into contact with the ridge: pinning, wetting and splashing. The effects of Weber number and the dimensionless distance between the impact point and the ridge are investigated, and a phase portrait of the different wetting outcomes is presented. For each of the potential outcomes, a side-by-side comparison of experimental and numerical results can be made. An energy balance approach is used to study the transitions between the different outcomes.

Keywords: Drop impact, Surface ridge, Drop wetting, High-speed photography, Lattice Boltzmann method

1. INTRODUCTION

Following impact of a liquid drop on to a solid surface, the liquid typically forms a thin lamella which spreads over the surface (Yarin 2006; Josserand Christophe and Thoroddsen 2016). Wetting outcomes are determined by parameters such as the surface roughness, impact velocity (V), drop size, liquid viscosity (μ) and surface tension (γ). Rioboo et al. identified five such outcomes: deposition, prompt splash, corona splash, receding breakup and rebound (Rioboo et al. 2001). To simplify and reduce the number of parameters, drop impact conditions can be characterized by the dimensionless Reynolds and Weber numbers, which balance inertial forces with viscous and capillary forces, respectively:

$$\mathrm{Re} = \frac{\rho V D_0}{\mu} \tag{1}$$

$$\mathrm{We} = \frac{\rho V^2 D_0}{\gamma} \tag{2}$$

Here D_0 denotes the diameter of the drop (assumed spherical for drops smaller than the capillary length).

Various researchers have drawn links between impact parameters and splashing (Rioboo et al. 2001; Xu 2007; Tsai et al. 2010; Kim et al. 2014), and it is known that splashing can be suppressed by reducing the ambient pressure (Tsai et al. 2010). Splash thresholds have been identified as a function of Weber number (Tsai et al. 2010) and surface morphology (Kim et al. 2014). When it comes to morphologies, research into drop impact on to rough and micropatterned solid surfaces is a growing area of interest (Kannan and Sivakumar 2008; Ellis et al. 2011; Marengo et al. 2011; Kim et al. 2012; Khojasteh et al. 2016), particularly when the surfaces are superhydrophobic. This research is often motivated by the prospect of being able to design patterns which can control impact outcomes.

When using micropatterns to design surfaces, it is important to understand the interaction between impacting drops and single topographic features. However, very little attention has been paid to how a moving contact line interacts with a single well-defined topographical feature. Josserand et al. performed experiments on the impact of a droplet on a Teflon-coated surface with a small obstacle placed in the droplet spreading path (Josserand C et al. 2005). In that study, the influence of the obstacle's thickness and distance from the impact point on the splashing angle were investigated, with Re and We held constant. Numerical simulations of these impacts were also carried out. Splashing was observed in the simulations, but the splashing angle for the simulations was smaller than in experiments. Jong et al. experimentally studied the impact of a drop near a millimeter-sized pit or pore (de Jong et al. 2015).

In this article, we present a combined experimental and numerical study of the wetting of a topographical feature after impact. This work should provide greater understanding of water drop impacts near individual topographic features. We focus on the interaction between the edge of the spreading lamella and a micron-scale ridge on an otherwise flat polymer surface (Fig. 1), including identification of the different possible wetting outcomes. This article aims to investigate the influence of two important control parameters on the wetting outcomes: the dimensionless distance from the impact point to the ridge (R/D_0) and the Weber number (Eq. 2). Impacts are studied experimentally using high-speed photography, and simulated using a two-dimensional (2D) multiphase lattice Boltzmann method. To explore the degree of

quantitative agreement between the simulations and the experiments, an analysis is carried out using simple energy conservation arguments relating to the maximum extent of drop spreading (Collings et al. 1990; Bennett and Poulikakos 1993; Wildeman et al. 2016).

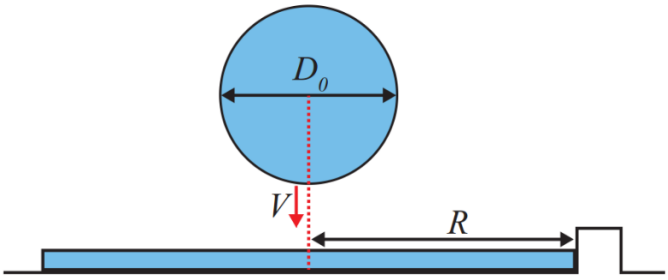

Fig. 1. Schematic of a drop impacting on a surface with a single ridge. D_0 denotes the initial diameter of the droplet, V denotes the impact velocity and R denotes the distance parallel to the surface from the edge of the ridge to the center of the droplet.

The lamella-ridge interaction is especially relevant in two areas of research that have recently been prominent in the literature. Firstly, researchers have noted the ability to reduce a droplet's contact time with a surface by direct impact on a thin hydrophobic ridge (Bird et al. 2013; Gauthier et al. 2015). In applications where the drop incidence is stochastic, droplets will commonly impact some distance away from a ridge, after which a spreading lamella will impact the ridge from the side (Regulagadda et al. 2017). A related problem is the spread of a lamella on or near vascular bundles (veins) on leaves, which can produce asymmetric drop outcomes (Fritsch et al. 2013). The second area of specific relevance concerns the interplay between spreading dynamics and the Cassie and Wenzel states, which are more familiar from quasi-static wetting. In the Cassie state (characteristic of superhydrophobic surfaces), the liquid is pinned on top of the surface microstructure, creating regions of liquid-air interface under the drop. In the Wenzel state, the liquid completely wets the microstructure. Drop impact experiments have shown that a lamella can transition from fully penetrating a microstructure to spreading over the top of the pillars (Reyssat et al. 2010; Tsai et al. 2011; Robson and Willmott 2016). This transition is similar to a lamella moving over a ridge, studied here.

The paper is organized as follows. The next section describes the experimental and numerical methodologies which have been implemented in this study. To identify the different possible outcomes, a side-by-side comparison of experimental and numerical results for each of three classified outcomes is depicted. Then full numerical and experimental results are presented, and the effects of control parameters on the outcome are discussed using a phase portrait. The final section presents concluding remarks.

2. METHODOLOGY

2.1. Experimental Methodology

Vertical drop impacts were recorded from a horizontal line of sight using a Photron SA5 high speed camera and Nikkor 105 mm macro lens. Back lighting was used to produce sharp contrast at the edge of the drop. A ridge with height 54 µm and width 41 µm was produced on a polydimethylsiloxane (PDMS) surface using soft lithography (Fig. 2). An acrylic (polymethyl methacrylate) substrate was spin coated with SU8-2050 (MicroChem Corp, USA) and exposed using a 375 nm direct mask writer (Heidelberg Instruments PG101, Germany). The ridge was cast from this mould using PDMS, and optical profilometry (Bruker ContourGT-K) was used to measure the geometry of the ridge. Fig. 2 (a) shows that the ridge walls are not perfectly vertical. The slope is calculated at 84.9°, near to the manufacturer's stated limit for the optical profiler (87° maximum slope angle). The ridge width was 41.2 ± 0.8 µm, where the uncertainty is determined by the limitations of the optical profiler. Water droplets were produced using a blunt 90° stainless steel gauge 24 needle (Cadence Science, USA), fed by a syringe pump (NE-1000, New Era Pump Systems Inc, USA). The needle was mounted on a custom built micrometer-based three-dimensional positioning system allowing for precise positioning of the droplet relative to the ridge.

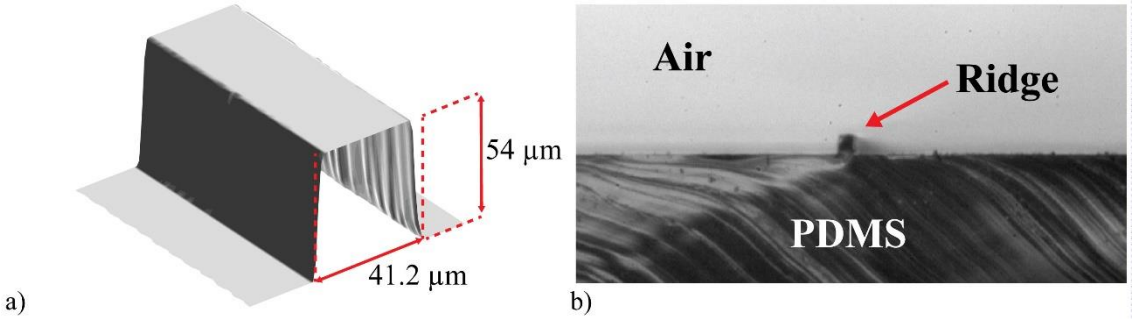

Fig. 2. (a) Optical profilometry of the ridge used in experiments. (b) Optical image of the ridge profile, obtained using an Infinity K2 DistaMax microscopic lens.

Drop impact videos were processed using a custom Matlab script. Image processing enables extraction of the trajectory of the droplet prior to impact, allowing calculation of D_0, V and R. Due to air resistance (Thoroddsen et al. 2005) and release conditions, droplets are not perfectly

spherical at impact, although the eccentricity is small (mean 1.02) so that the effect on drop outcomes should be minimal (Mishra et al. 2011). D_0 is calculated by assuming that the drop is ellipsoidal, and finding the diameter of a sphere with equal volume. D_0 was typically 2-3 mm in diameter, while R/D_0 was more widely varied by adjusting the point of impact. By altering the height of the drop, impact Weber numbers were adjusted from approximately 25 to 400. Weber number was calculated using (Eq. 2) and values of surface tension and density were obtained from (Kell 1975; Vargaftik et al. 1983). We use Weber number to characterise the impacts because the outcomes should be predominantly governed by competition between the kinetic and surface energies; there is a monotonic relationship between Weber and Reynolds numbers for water drops (Eq. 1).

2.2. Numerical Method

The Lattice Boltzmann Method (LBM) originated from the cellular automata concept which was discovered by Ulam and von Neumann in the 1940s (Sukop and Thorne Jr 2006). Zhang has reported an exhaustive review of the development of LBM for microfluidics (Zhang 2011). The transport Boltzmann equation based on the BGK approximation can be written as

$$\frac{\partial f}{\partial t} + \boldsymbol{e}\,\nabla f = \frac{f^{eq} - f}{\tau} \tag{3}$$

where $f(\boldsymbol{x}, \boldsymbol{e}, t)$ and $f^{eq}(\boldsymbol{x}, t)$ are the particle distribution function and the equilibrium distribution function, respectively. $\boldsymbol{x}$ denotes the position and $\boldsymbol{e}$ is the microscopic velocity. τ represents the relaxation time. During our simulations, the default value of the relaxation time is unity. The main idea behind the LBM is to solve the following discrete Boltzmann equation:

$$f_k(\boldsymbol{x} + \boldsymbol{e}_k \Delta t\,, t + \Delta t) - f_k(\boldsymbol{x}, t) = \frac{\Delta t}{\tau}[f_k^{eq}(\boldsymbol{x}, t) - f_k(\boldsymbol{x}, t)] \tag{4}$$

This can be solved numerically using a two-stage process. The first step is the streaming step, which models the particle distribution advection along the lattice link,

$$f_k(x + \Delta x\,, y + \Delta y, t + \Delta t) = f_k(x\,, y, t + \Delta t) \tag{5}$$

and the following step is the collision step, which models the rate of change in the particle distribution,

$$f_k(x\,, y, t + \Delta t) = f_k(x\,, y, t) + \frac{\Delta t}{\tau}[f_k^{eq}(x\,, y, t) - f_k(x\,, y, t)] \tag{6}$$

In this work, we choose the D2Q9 model as shown in Fig. 3 which has nine discrete velocities $\boldsymbol{e}_k$ such that $k = 0, \ldots, 8$ in two dimensions:

$$[\boldsymbol{e}_0, \boldsymbol{e}_1, \boldsymbol{e}_2, \boldsymbol{e}_3, \boldsymbol{e}_4, \boldsymbol{e}_5, \boldsymbol{e}_6, \boldsymbol{e}_7, \boldsymbol{e}_8] = c \begin{bmatrix} 0 & 1 & 0 & -1 & 0 & 1 & -1 & -1 & 1 \\ 0 & 0 & 1 & 0 & -1 & 1 & 1 & -1 & -1 \end{bmatrix} \tag{7}$$

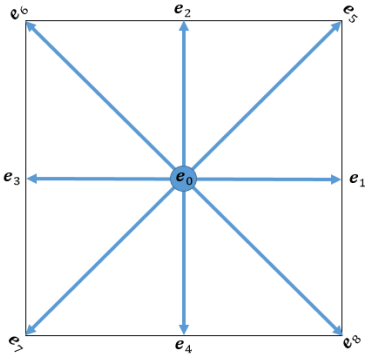

Fig. 3. Discrete velocity model D2Q9 which consists of nine velocities ($\boldsymbol{e}_k$ where k= 0, 1,…, 8) in two dimensions. $\boldsymbol{e}_0$ defines particles at rest. The lattice unit (lu) and the time step (ts) are basic units for the length and the time, respectively. The x and y components of velocities are either 0 or ±1 and therefore the magnitude of velocity for $\boldsymbol{e}_1$ to $\boldsymbol{e}_4$ is 1 ($lu.ts^{-1}$) and for $\boldsymbol{e}_5$ to $\boldsymbol{e}_8$ is $\sqrt{2}$ ($lu.ts^{-1}$).

In Eq. 7, c denotes the lattice speed and is calculated by $c = \frac{\Delta x}{\Delta t}$ where $\Delta x = 1$ lattice unit (lu) and $\Delta t = 1$ time step (ts). For the D2Q9 velocity model, the equilibrium distribution function is defined as:

$$f_k^{eq}(\boldsymbol{x}, t) = \omega_k \rho[1 + 3(\boldsymbol{c}_k.\boldsymbol{u}) + \frac{9}{2}(\boldsymbol{c}_k.\boldsymbol{u})^2 - \frac{3}{2}\boldsymbol{u}^2) \tag{8}$$

where $\boldsymbol{u}$ denotes the macroscopic velocity and ω is the weight factor which is 4/9 for k=0, 1/9 for k=1,2,3,4 is and 1/36 for k=5,6,7,8.

The kinematic viscosity is a function of the relaxation time and can be determined by $\upsilon = c_s^2(\tau - 0.5)\Delta t$ where c_s denotes the sound speed which can be obtained from $c_s^2 = \frac{c^2}{3}$ in the D2Q9 model. In simulations, any lattice nodes can be occupied by either a fluid (gas or liquid) node or a solid node. Boundary conditions applied include the bounce-back boundary condition at the solid-liquid interface in the collision step, and the periodic boundary condition for other boundaries in the streaming step. In the LBM, the bounce back boundary is implemented as the known distribution function (from the streaming process) hits the wall and bounces back to the region. The periodic boundary condition is implemented by requiring that as the distribution function reaches the end of the region, f_k carries over on to the opposite wall. The macroscopic fluid density ρ and the macroscopic velocity $\boldsymbol{u}$ can be calculated as:

$$\rho = \sum_{k=0}^{8} f_k \tag{9}$$

$$\rho \boldsymbol{u} = \sum_{k=0}^{8} f_k \, \boldsymbol{e}_k \tag{10}$$

In this study, we use the single component multiphase Shan Chen model (SCMP) (Shan and Chen 1993). In this model, the inclusion of the inter-particle force modifies the pressure term to the non-ideal and non-monotonic equation of state (EOS). The inter-particle forces between the solid node and fluid node (adhesive force) and also between fluid nodes (cohesive force) are calculated using the Shan-Chen model:

$$\boldsymbol{F}(\boldsymbol{x}, t) = -G\psi(\boldsymbol{x}, t) \sum_{k=0}^{8} \omega_k \psi(\boldsymbol{x} + \boldsymbol{e}_k \Delta t, t) \boldsymbol{e}_k \tag{11}$$

where G is a parameter controlling the strength of the inter-particle force. In the simulation, this parameter acts analogously to an inverse temperature scale and creates the liquid-gas interface with constant surface tension, density gradient and interface thickness. ψ denotes an interaction potential (pseudopotential) to model attraction and repulsion between the phases and can be calculated as:

$$\psi(\rho) = \sqrt{\frac{2(P - c_s^2 \rho)}{c_s^2 G}} \tag{12}$$

where P denotes pressure and can be obtained using the pressure-density relation by the Carnahan and Starling (C-S) equation of state:

$$P = \rho \lambda T \frac{1 + \frac{\beta\rho}{4} + (\frac{\beta\rho}{4})^2 - (\frac{\beta\rho}{4})^3}{(1 - \frac{\beta\rho}{4})^3} - \alpha\rho^2 \tag{13}$$

where T denotes the temperature and is equal T =0.0943T_0 according to $\alpha = 1 \ lu^5/(mu.ts^2)$, $\beta = 4 \ lu^3/mu$ and $\lambda = 1 \ lu^2/(ts^2 . tu)$ (Yuan and Schaefer 2006). Furthermore, in this model, we can obtain the interaction between the fluids and the wall by giving the solid nodes an artificial wall density ρ_w where $\rho_g \leq \rho_w \leq \rho_l$ (Benzi et al. 2006). ρ_g and ρ_l denote the gas and liquid density and in our simulation are chosen to be 0.0285 ($^{mu}/_{lu^3}$) and 0.285 ($^{mu}/_{lu^3}$),

respectively. In the SCMP, the equilibrium distribution function is updated using the equilibrium velocity. This equilibrium velocity $\boldsymbol{u}^{eq}$ which replaces u in Eq. 8 can be determined as:

$$\boldsymbol{u}^{eq} = \boldsymbol{u} + \frac{\boldsymbol{F}\tau}{\rho} \tag{14}$$

According to the above explanation, a FORTRAN code has been developed in two-dimensional space. In our simulations, the effects of gravity are neglected. The numerical algorithm consists of three main stages, which are an initialisation stage including initialising variables and nodes; a main loop including the collision step, the streaming step, boundary conditions, calculating macroscopic quantities, determining forces and obtaining the equilibrium velocity; and finally a post-processing stage including plotting the density contours. The validity of this Lattice-Boltzmann method for drop impacts was demonstrated in (Rashidian and Sellier 2017) where it was shown that the maximum spread radius reproduces well the well-known correlation of (Scheller and Bousfield 1995) for impact on flat, non-textured surfaces.

3. RESULTS AND DISCUSSION

3.1. Classification of outcomes

We define the outcome of the drop impact at the moment when the lamella is at maximum spread, immediately prior to recoil. Three basic outcomes have been observed. Firstly, the advance of the lamella may be arrested before the drop reaches the far side of the ridge, an outcome labelled as pinning (Fig. 4). For pinning, the lamella may spread and touch the ridge without extending horizontally beyond the ridge, or it may extend beyond it, but it must start to recoil prior to touching the surface on the other side. Wetting, the second outcome, occurs when the drop spreads on to the surface beyond the ridge without breaking up (Fig. 5). In some wetting cases, the lamella first makes contact with the surface on the far side at some distance from the edge of the ridge. The third outcome is splashing, when smaller drops are generated from the lamella edge while the lamella is in contact with the ridge, prior to the onset of lamella retraction (Fig. 6).

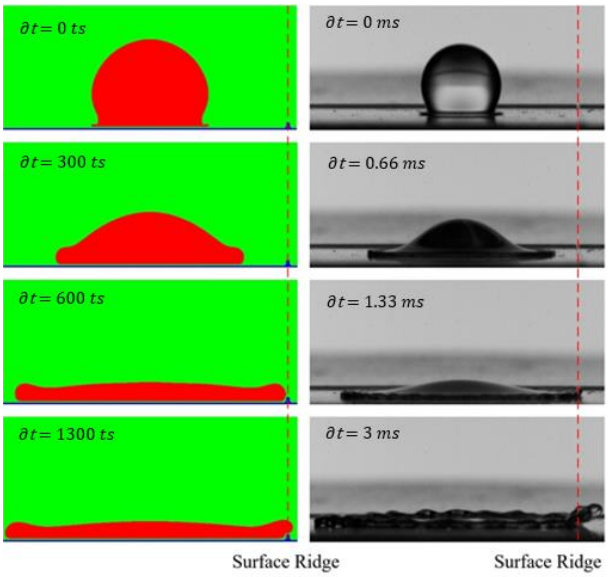

Fig. 4. Side-by-side comparison of numerical (left) and experimental (right) results for the pinning outcome, both obtained for $\frac{R}{D_0}$=1.48 and We=144. In the photographs, the red dashed line indicates the position of the ridge.

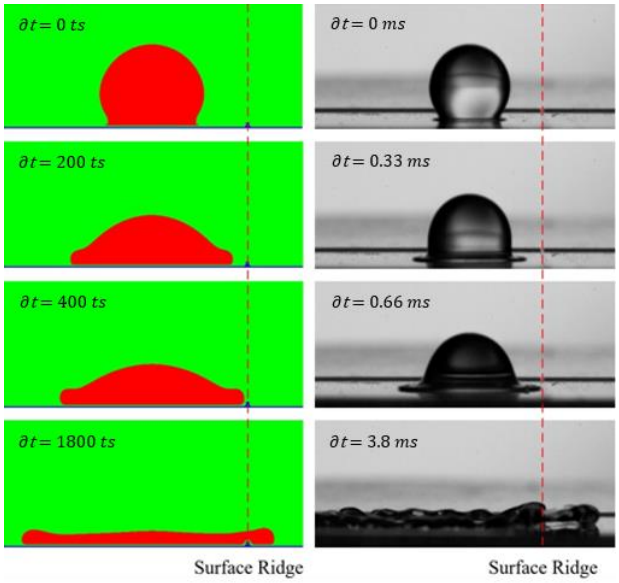

Fig. 5. Side-by-side comparison of numerical (left) and experimental (right) results for the wetting outcome, both obtained for $\frac{R}{D_0}$=0.91 and We=142. In the photographs, the red dashed line indicates the position of the ridge.

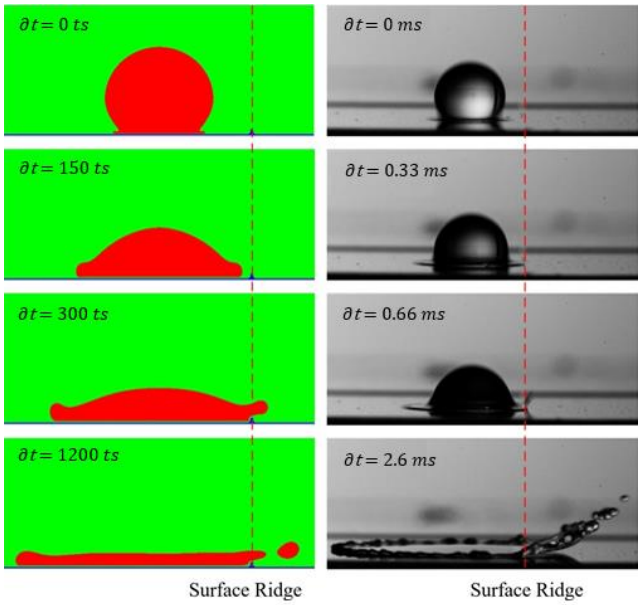

Fig. 6. Side-by-side comparison of numerical (left) and experimental (right) results for the splashing outcome, both obtained for $\frac{R}{D_0}$=0.86 and We=237. In the photographs, the red dashed line indicates the position of the ridge.

Figs. 4, 5 and 6 provide a side-by-side comparison for the three different outcomes. In each figure, four steps during droplet impact are shown: (i) impact (∂t = 0), when the droplet strikes the surface; (ii) as the droplet begins to spread; (iii) when the droplet first touches the ridge; and (iv) the droplet at maximum spread, when the outcome of the impact is determined. Simulations and experiments show good qualitative agreement, although there are observable differences. For example, in Fig. 6 the simulated splashing angle is smaller than the angle observed in experiments, an observation previously reported by Josserand et al (Josserand C et al. 2005). It can also be seen that the size of the satellite drop in simulations is larger than the ejected drops in experiments. Moreover, free surface perturbations can be observed experimentally in the wetting case, while these are absent in simulations. Several factors may explain these differences. Firstly, simulations are 2D; this point will be discussed further in the next section. Secondly, the density ratio in simulations is significantly different from the experimental case due to limitations of the SCMP lattice Boltzmann method (Huang et al. 2011). It should be noted that simulations have the density ratio of 10, whereas this ratio is 1000 for experiments. Thus simulations are not able to capture the smaller length scale effects entirely.

3.2. Energy approach for analysing transitions

When the droplet meets the ridge, the outcome should be predominantly governed by competition between the kinetic and surface energies, noting that the Bond number of the

droplets (equal to $\rho g D_0^2 / 4\gamma$ for gravitational acceleration g) was typically less than 0.30. Therefore, a simple energy balance approach is used to study the dependence of the pinning-wetting transition on $\frac{R}{D_0}$ and We. The model is based on an estimate for the maximum spread of an impacting droplet (Collings et al. 1990; Bennett and Poulikakos 1993), in which the reduction in kinetic energy following impact is equated to the extra surface energy produced in deforming the droplet. This analysis allows us to compare 2D and 3D models, and therefore to address the differences between the experimental and simulation data. The method is approximate because energy losses due to viscous dissipation (known to be significant in drop spreading (Wildeman et al. 2016)) are neglected, and because the spreading drop is modelled as a cylindrical disc with the liquid-vapour surface tension applicable on all surfaces. However, we do account for the initial surface energy, which was neglected in Collings et al.'s model (Collings et al. 1990) that yields the widely-used result that the maximum spreading diameter scales $\propto \mathrm{We}^{0.5}$ (Marengo et al. 2011). Regarding viscous losses, it has been found that approximately half of initial kinetic energy is transformed to surface energy during drop impact, independent of impact parameters (Wildeman et al. 2016), suggesting that a model with one or two parameters can accurately capture the spreading behaviour.

For this energy balance approach, the kinetic energy and surface energy prior to impact are equated to the sum of these energies when the drop has spread. If a 2D droplet of density ρ (unit kg.m^{-1}) and surface tension γ (unit J.m^{-1}) spreads to its maximum extent, forming a rectangle of height h and length L, this energy balance gives:

$$\frac{1}{2}\rho V^2 \pi \left(\frac{D_0}{2}\right)^2 + \pi D_0 \gamma = KE_f + 2\gamma(h + L) \tag{15}$$

where KE_f is the final kinetic energy, which is zero at maximum spread. Using volume conservation due to incompressibility ($hL = \pi {D_0}^2/_4$), we then find:

$$\frac{\pi}{8}\rho V^2 {D_0}^2 = \gamma\left(\frac{\pi {D_0}^2}{2L} + 2L - \pi D_0\right) \tag{16}$$

or using Eq. 2,

$$\mathrm{We} = \frac{16L}{\pi D_0} + \frac{4 D_0}{L} - 8 \tag{17}$$

In this investigation, we assume that the pinning-wetting transition occurs at some spreading diameter smaller than L, so that $2R = NL$ where $0 < N \leq 1$. Using the constant N allows us to

make a simple fit to the experimental and simulated data. Using this relation with Eq. 17, we obtain for the 2D case:

$$\mathrm{We} = \frac{32R}{N\pi\, D_0} + \frac{2N\, D_0}{R} - 8 \tag{18}$$

In 3D, if the drop at maximum spread forms a cylindrical disc of height h and diameter L, the energy balance is:

$$\frac{1}{2}\rho V^2 \frac{4}{3}\pi\left(\frac{D_0}{2}\right)^3 + 4\pi\gamma\left(\frac{D_0}{2}\right)^2 = KE_f + \pi\gamma(hL + \frac{L^2}{2}) \tag{19}$$

As in the 2D case, we consider the point of maximum spread (KE_f = 0), use conservation of volume due to incompressibility ($\pi h(L/2)^2 = \pi\ {D_0}^3/6$) and assume that the transition occurs at $2R = ML$ for some constant M where $0 < M \leq 1$. Following Eq. 19, we obtain Eq. 20 for the 3D case. For control experiments of water droplet impact on flat PDMS surfaces (80 < We < 230), the maximum spread is described by Eq. 20 with M = 1.334.

$$\mathrm{We} = \frac{24R^2}{M^2\ {D_0}^2} + \frac{4MD_0}{R} - 12 \tag{20}$$

3.3. Phase portrait of outcomes

A phase portrait of the experimental and simulated wetting outcomes is shown in Fig. 7. Simulations matching the experiments were carried out over the range 25 < We < 350, and for impact points such that $0.5 \leq R/D_0 \leq 2$. Note that if $R/D_0 \leq 0.5$, part of the drop lands directly on the ridge, a situation not studied here.

Describing the thresholds for transition between the pinned, wetting and splashing outcomes is of particular interest. Solid lines indicate transitions from pinned to wetting outcomes in both simulations and experimental results. Dashed lines show transitions from wetting to splash outcomes. For the experimental cases, lines are fitted with a least squares method to calculate the best value of M using Eq. 20. For the simulations, a similar method was used to find N, although Eq. 18 was modified to

$$\mathrm{We} = \frac{32R}{N\pi D_0} + \frac{2ND_0}{R} - 8 - S \tag{21}$$

Inclusion of the constant parameter S is necessary because the simple 2D model, Eq. 18, gives imaginary values of R/D_0 near the origin ($\mathrm{We} < 17$). Physically, this is because the model does not account for spreading driven by gravity or surface-liquid interactions at low We.

Firstly considering the boundary between the pinning and wetting outcomes in Fig. 7, it is clear that the energy required to submerge the ridge is reduced as the distance from the ridge decreases. The 3D fit using our simple model gives a good description of the experimental transition, and predicts that the transition occurs at slightly less than half the distance to maximum spread. Eq. 20 gives $R/D_0 \propto \mathrm{We}^{0.5}$ to first order, in agreement with the widely used results for maximum spread which uses a similar analytic approach (Collings et al. 1990).

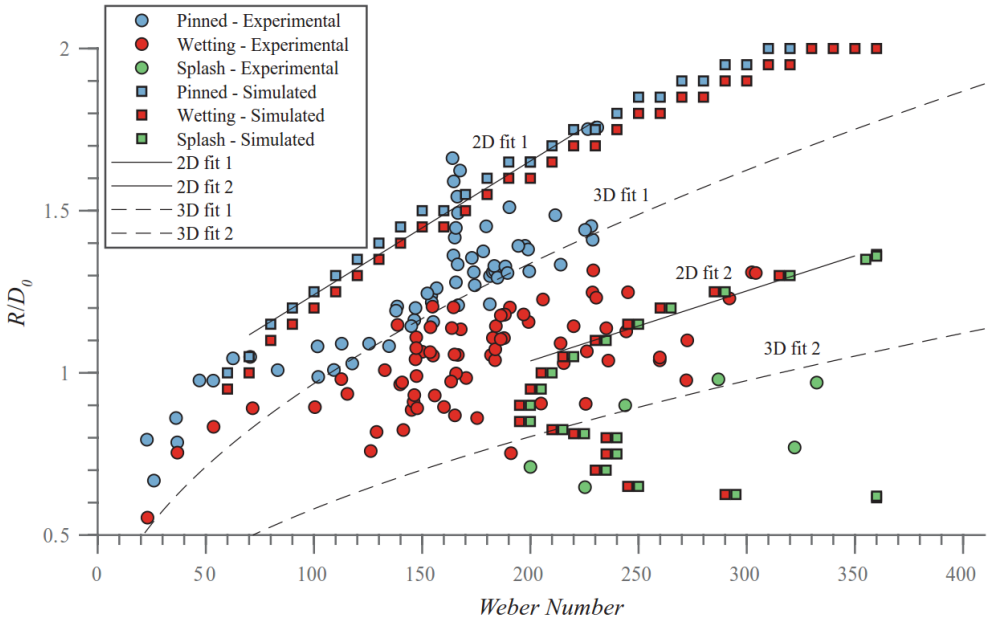

Fig.7. Phase portrait of the wetting outcomes. The solid lines are fits to the simulation data using a 2D model over the ranges of Weber number shown (Eq. 21. Fit1: N=0.042, S=193. Fit 2: N=0.022, S=272). The dashed lines are fits to the experimental data using a 3D model (Eq. 20. Fit1: M=0.45. Fit 2: M=0.27).

Qualitatively, the experimental results are consistent with simulations, although direct quantitative comparison is not appropriate because the simulations are carried out in 2D. For example, the spreading 2D drop meets the ridge along a line, whereas the 3D drop first touches the ridge at a point. The fit to the simulation data using the 2D model (Eq. 21) can be used to effectively describe the pinning/wetting transition over a limited range of We. The model is limited by the lack of a solution at low We (mentioned above), and because viscous effects have been neglected.

Similar results are obtained for the transition from wetting to splash in Fig. 7. The closer to the ridge the droplet impacts, the more likely it is to retain enough energy after

surmounting the ridge to break up into droplets. The experimental data suggest that this transition occurs when the ridge is about 0.27 of the distance to theoretical maximum spread.

Interestingly the simulation data are non-monotonic, and suggest that a wetting to splashing transition occurs at low value of R/D_0. In the simulations, drops travelling at high velocity and landing close to the ridge immediately wet the surface beyond the ridge, and do not break up. When a drop has slightly further to travel before reaching the ridge, it will break up and splash. This transition was not observed in experiments, and probably reflects the importance of inertia and small length scales in the drop breakup dynamics when the drop lands very near the ridge. It is also possible that wetting outcomes (without splashing) could be observed in experiments close to $R/D_0 = 0.5$ at high We. The upper branch of the simulated wetting-splashing transition is qualitatively similar to the experimental result, although quantitative agreement is not found for similar reasons to the pinning-wetting transition.

The analytic approach used to define the transitions in Fig. 7 has recognized limitations (Marengo et al. 2011), in addition to the issue noted above for the 2D case at low We. In particular, viscous dissipation is neglected, and this generally accounts for about half the energy loss in more sophisticated analytical approaches (Wildeman et al. 2016). Also, our approach has not accounted for the surface energy at the solid-liquid interface. A comparison with the model at the Collings et al. (Collings et al. 1990) which includes the contact angle for a spherical cap, suggests that this omission would not strongly affect the results we have obtained.

4. CONCLUSION

In this study, we have used the multiphase Lattice Boltzmann method and high-speed imaging to investigate the interaction between the edge of an impacting water drop and a microscopic polymer ridge. Experimental and simulation outcomes have been categorised as pinning, wetting and splashing when the lamella is at maximum spread. A simple model based on energy conservation has been developed to predict experimental outcomes as a function of the Weber number and the distance from the impact point to the ridge. This model ($R/D_0 \propto \mathrm{We}^{0.5}$ to first order) gives a good description of the pinning-wetting and wetting-splashing transitions. The model could be improved by including viscous and gravitational contributions. Identification of these transitions can assist with the study and design of surface microstructures which passively control the outcomes of drop impact events.

When comparing the 2D numerical results with the experimental data, there is good qualitative agreement for each of the three classified outcomes. There is a clear pathway towards improvement of the simulations based on comparison with the experiments. For example, differences in the wetting front dynamics were observed because the simulations do not entirely capture smaller length scale effects (the simulations assumed a liquid to gas density ratio of 10 which is smaller than the density ratio of 1000 in experiments). The 2D energy conservation model only produces a reasonable fit to transition thresholds over limited ranges of Weber number. Lack of quantitative agreement is to be expected because of the 2D nature of the simulations. Despite these drawbacks to the simulations implemented here, the multiphase lattice Boltzmann method remains a very powerful tool to unravel wetting phenomena such as drop impact, and has provided useful insights here.

5. REFERENCES

Bennett T, Poulikakos D. 1993. Splat-quench solidification: estimating the maximum spreading of a droplet impacting a solid surface. Journal of Materials Science. 28(4):963-970.

Benzi R, Biferale L, Sbragaglia M, Succi S, Toschi F. 2006. Mesoscopic modeling of a two-phase flow in the presence of boundaries: the contact angle. Physical Review E. 74(2):021509.

Bird JC, Dhiman R, Kwon H-M, Varanasi KK. 2013. Reducing the contact time of a bouncing drop. Nature. 503(7476):385.

Collings E, Markworth A, McCoy J, Saunders J. 1990. Splat-quench solidification of freely falling liquid-metal drops by impact on a planar substrate. Journal of Materials Science. 25(8):3677-3682.

de Jong R, Enríquez OR, van der Meer D. 2015. Exploring droplet impact near a millimetre-sized hole: comparing a closed pit with an open-ended pore. Journal of fluid mechanics. 772:427-444.

Ellis A, Smith F, White A. 2011. Droplet impact on to a rough surface. The Quarterly Journal of Mechanics & Applied Mathematics. 64(2):107-139.

Fritsch A, Willmott G, Taylor M. 2013. Superhydrophobic New Zealand leaves: contact angle and drop impact experiments. Journal of the Royal Society of New Zealand. 43(4):198-210.

Gauthier A, Symon S, Clanet C, Quéré D. 2015. Water impacting on superhydrophobic macrotextures. Nature communications. 6:8001.

Huang H, Krafczyk M, Lu X. 2011. Forcing term in single-phase and Shan-Chen-type multiphase lattice Boltzmann models. Physical Review E. 84(4):046710.

Josserand C, Lemoyne L, Troeger R, Zaleski S. 2005. Droplet impact on a dry surface: triggering the splash with a small obstacle. Journal of fluid mechanics. 524:47-56.

Josserand C, Thoroddsen ST. 2016. Drop impact on a solid surface. Annual review of fluid mechanics. 48:365-391.

Kannan R, Sivakumar D. 2008. Drop impact process on a hydrophobic grooved surface. Colloids and Surfaces A: Physicochemical and Engineering Aspects. 317(1-3):694-704.

Kell GS. 1975. Density, thermal expansivity, and compressibility of liquid water from 0. deg. to 150. deg.. Correlations and tables for atmospheric pressure and saturation reviewed and expressed on 1968 temperature scale. Journal of Chemical and Engineering data. 20(1):97-105.

Khojasteh D, Kazerooni M, Salarian S, Kamali R. 2016. Droplet impact on superhydrophobic surfaces: A review of recent developments. Journal of Industrial and Engineering Chemistry. 42:1-14.

Kim H, Lee C, Kim MH, Kim J. 2012. Drop impact characteristics and structure effects of hydrophobic surfaces with micro-and/or nanoscaled structures. Langmuir. 28(30):11250-11257.

Kim H, Park U, Lee C, Kim H, Hwan Kim M, Kim J. 2014. Drop splashing on a rough surface: How surface morphology affects splashing threshold. Applied Physics Letters. 104(16):161608.

Marengo M, Antonini C, Roisman IV, Tropea C. 2011. Drop collisions with simple and complex surfaces. Current Opinion in Colloid & Interface Science. 16(4):292-302.

Mishra NK, Zhang Y, Ratner A. 2011. Effect of chamber pressure on spreading and splashing of liquid drops upon impact on a dry smooth stationary surface. Experiments in fluids. 51(2):483-491.

Rashidian H, Sellier M. 2017. Modeling an impact droplet on a pair of pillars. Interfacial Phenomena and Heat Transfer. 5(1).

Regulagadda K, Bakshi S, Das SK. 2017. Morphology of drop impact on a superhydrophobic surface with macro-structures. Physics of Fluids. 29(8):082104.

Reyssat M, Richard D, Clanet C, Quéré D. 2010. Dynamical superhydrophobicity. Faraday discussions. 146:19-33.

Rioboo R, Tropea C, Marengo M. 2001. Outcomes from a drop impact on solid surfaces. Atomization and sprays. 11(2).

Robson S, Willmott GR. 2016. Asymmetries in the spread of drops impacting on hydrophobic micropillar arrays. Soft matter. 12(21):4853-4865.

Scheller BL, Bousfield DW. 1995. Newtonian drop impact with a solid surface. AIChE Journal. 41(6):1357-1367.

Shan X, Chen H. 1993. Lattice Boltzmann model for simulating flows with multiple phases and components. Physical Review E. 47(3):1815.

mSukop M, Thorne Jr D. 2006. Lattice Boltzmann modeling: an introduction for geoscientists and engineers. Springer.

Thoroddsen S, Etoh T, Takehara K, Ootsuka N, Hatsuki Y. 2005. The air bubble entrapped under a drop impacting on a solid surface. Journal of Fluid Mechanics. 545:203-212.

Tsai P, CA van der Veen R, van de Raa M, Lohse D. 2010. How micropatterns and air pressure affect splashing on surfaces. Langmuir. 26(20):16090-16095.

Tsai P, Hendrix MH, Dijkstra RR, Shui L, Lohse D. 2011. Microscopic structure influencing macroscopic splash at high Weber number. Soft Matter. 7(24):11325-11333.

Vargaftik N, Volkov B, Voljak L. 1983. International tables of the surface tension of water. Journal of Physical and Chemical Reference Data. 12(3):817-820.

Wildeman S, Visser CW, Sun C, Lohse D. 2016. On the spreading of impacting drops. Journal of fluid mechanics. 805:636-655.

Xu L. 2007. Liquid drop splashing on smooth, rough, and textured surfaces. Physical Review E. 75(5):056316.

Yarin AL. 2006. Drop impact dynamics: splashing, spreading, receding, bouncing…. Annu Rev Fluid Mech. 38:159-192.

Yuan P, Schaefer L. 2006. Equations of state in a lattice Boltzmann model. Physics of Fluids. 18(4):042101.

Zhang J. 2011. Lattice Boltzmann method for microfluidics: models and applications. Microfluidics and Nanofluidics. 10(1):1-28.

Figure captions

Fig. 8. Schematic of a drop impacting on a surface with a single ridge. D_0 denotes the initial diameter of the droplet, V denotes the impact velocity and R denotes the distance parallel to the surface from the edge of the ridge to the center of the droplet.

Fig. 9. (a) Optical profilometry of the ridge used in experiments. (b) Optical image of the ridge profile, obtained using an Infinity K2 DistaMax microscopic lens.

Fig. 10. Discrete velocity model D2Q9 which consists of nine velocities ($\boldsymbol{e}_k$ where k= 0, 1,…, 8) in two dimensions. $\boldsymbol{e}_0$ defines particles at rest. The lattice unit (lu) and the time step (ts) are basic units for the length and the time, respectively. The x and y components of velocities are either 0 or ±1 and therefore the magnitude of velocity for $\boldsymbol{e}_1$ to $\boldsymbol{e}_4$ is 1 ($lu.ts^{-1}$) and for $\boldsymbol{e}_5$ to $\boldsymbol{e}_8$ is $\sqrt{2}$ ($lu.ts^{-1}$).

Fig. 11. Side-by-side comparison of numerical (left) and experimental (right) results for the pinning outcome, both obtained for $\frac{R}{D_0}$=1.48 and We=144. In the photographs, the red dashed line indicates the position of the ridge.

Fig. 12. Side-by-side comparison of numerical (left) and experimental (right) results for the wetting outcome, both obtained for $\frac{R}{D_0}$=0.91 and We=142. In the photographs, the red dashed line indicates the position of the ridge.

Fig. 13. Side-by-side comparison of numerical (left) and experimental (right) results for the splashing outcome, both obtained for $\frac{R}{D_0}$=0.86 and We=237. In the photographs, the red dashed line indicates the position of the ridge.

Fig.14. Phase portrait of the wetting outcomes. The solid lines are fits to the simulation data using a 2D model over the ranges of Weber number shown (Eq. 21. Fit1: N=0.042, S=193. Fit 2: N=0.022, S=272). The dashed lines are fits to the experimental data using a 3D model (Eq. 20. Fit1: M=0.45. Fit 2: M=0.27).